Published in final edited form as:
*Nucl Instrum Methods Phys Res A*. 2011 October 1; 652(1): 731–734. doi:10.1016/j.nima.2010.09.116.

# A SPECT Camera for Combined MRI and SPECT for Small Animals

**D. Meier**[a,*], **D. J. Wagenaar**[b], **S. Chen**[c], **J. Xu**[c], **J. Yu**[c], and **B. M. W. Tsui**[c]

[a]Gamma Medica - Ideas (Norway) AS, Martin Linges Vei 25, Snarøya, POB 1, N-1330 Fornebu, Norway

[b]Gamma Medica - Ideas, Inc.,19355 Business Center Dr., Ste 8, 91324 Northridge, United States

[c]Department of Radiology, Johns Hopkins School of Medicine, Baltimore, MD, United States

## Abstract

We describe an MR-compatible SPECT camera for small animals. The SPECT camera system can be inserted into the bore of a state-of-the-art MRI system and allows researchers to acquire tomographic images from a mouse in-vivo with the MRI and the SPECT acquiring simultaneously. The SPECT system provides functional information, while MRI provides anatomical information. Until today it was impossible to operate conventional SPECT inside the MRI because of mutual interference. The new SPECT technology is based on semiconductor radiation sensors (CZT, ASICs), and it fits into conventional high field MRI systems with a minimum 12-cm bore size. The SPECT camera has an MR-compatible multi-pinhole collimator for mice with a ø25-mm field-of-view. For the work reported here we assembled a prototype SPECT camera system and acquired SPECT and MRI data from radioactive sources and resolution phantoms using the camera outside and inside the MRI.

### Keywords

SPECT; MRI; molecular imaging; multi-modality imaging

## 1. Introduction

SPECT provides tomographic images by measuring the intensity of $\gamma$-radiation from radio-nuclei attached to specific compound molecules. MRI systems also provide tomographic images, however, using signals from atomic nuclei that are spatially encoded by magnetic field gradients. The high magnetic field strengths of clinical and pre-clinical MRI preclude the use of conventional PMT based SPECT. Our solution is to replace PMTs and scintillators with MR-compatible cadmium zinc telluride (CZT) and to minimize the mutual interference between the SPECT and MRI systems.

Fig. 1 shows a diagram of the combined SPECT/MRI with the SPECT located inside the MRI bore. The combined SPECT/MRI modalities can provide co-registered images with



*Tel. +47 67 82 71 71 dirk.meier@gm-ideas.com (D. Meier).

complementary information. Table 1 lists potential synergies arising from a combined SPECT and MRI system.

There are three general areas of applications in the pre-clinical area: disease-based imaging, therapy response imaging, and emerging molecular imaging methods. In all three areas there are many applications that would benefit from a combined SPECT and MRI system [1]. Table 2 lists keywords of a few applications.

## 2. Instrumentation

Fig. 2 shows the SPECT camera in a cradle, and Table 3 lists the preliminary specifications. The outer diameter allows one to fit the SPECT camera inside a 12-cm bore of pre-clinical MRI systems. The use with a cradle is optional for the use of the SPECT inside large-bore MR systems or as a stand-alone system.

The radiation detector uses cadmium zinc telluride (CZT) and application specific integrated circuits (ASICs) [2,3]. A multi-pinhole radiation collimator sleeve and RF-coil, similar to Ref. [4], is mounted inside the SPECT camera. The collimator sleeve is made from a dense metal powder with precise keel-edge apertures for radiation collimation. The $\gamma$-radiation casts projection images through the apertures onto the detector modules. The principles of pinhole collimation and image formation are well known, where the sensitivity ($s$) and the spatial resolution ($r$) are important benchmarks of the SPECT imaging system. The detector sensitivity with a single aperture is $s=\frac{\varepsilon d^2\cos^3(\psi)}{16b^2}$, where $\varepsilon$ is the absorption probability in the detector, $d$ is the effective aperture diameter, $\psi$ is the angle between the incident ray and the pinhole normal, and $b$ is the length between the radiation source and the aperture center projected onto the pinhole normal [5]. *E.g.*: with $\varepsilon = 0.85$ (for 140-keV energy photons in 5-mm CZT), $b = 18.5$ mm and $\psi = 0$, one calculates 0.062% sensitivity for a ø2-mm effective aperture diameter.

The spatial resolution in the FoV due to the detector and the aperture combined is $r=\sqrt{\frac{\sigma^2}{M^2}+\left(1+\frac{1}{M}\right)^2 d^2}$, where $\sigma$ is the intrinsic spatial resolution and $M$ is the magnification. The magnification is defined as the ratio of the size of the projection of the object to its actual size. *E.g.*: with $M = 0.85$ (at the center of the FoV) and $\sigma = 1.6$ mm one calculates 2.2 mm FWHM spatial resolution for a ø0.5-mm aperture.

Conventional SPECT systems acquire multiple projections by rotating one or two planar cameras around the object. Fig. 3 illustrates the principle of our static SPECT system. Each octagon is fixed at a different tilt angle, and thereby provides projection views simultaneously and, unlike conventional SPECT, without any rotation. The projection data allows us to compute tomographic images. Each pinhole (index $k$) has sensitivity $s_k$. The overall sensitivity for $K$ pinholes is $S=\Sigma_k^K s_k$ Compared to a single pinhole, many pinholes with non-overlapping projections greatly increase the sensitivity. It is easily possible, if needed, to increase the number of angular samples by rotating the collimator around its axis.

We have developed methods for calibration and tomographic image reconstruction, and implemented the image reconstruction based on iterative maximum-likelihood expectation maximization (ML-EM) [6,7].

# 3. Results

## 3.1. γ-Energy Spectroscopy

The detector modules provide excellent energy resolution in all channels - a feature that increases image contrast and enables imaging of multiple isotopes with photon emissions at different energies simultaneously. We acquired energy spectra from $^{99m}$Tc $\gamma$-radiation using our SPECT camera inside the 3-T MRI system and at earth magnetic field strength. The axis of the SPECT camera inside the MRI was parallel to the 3-T magnetic field. Fig. 4 shows 2 energy spectra in units of the analog-to-digital converter (ADU) from the same detector element superimposed for 0 T and 3 T. One can see the 140-keV photopeak from $^{99m}$Tc and the 59-keV and 68-keV x-ray fluorescence emissions from the collimator material. The position of the peaks remains constant at 0 T and 3 T. The 2 spectra were normalized to the same peakheight to compare their spectral shape. One can see that the spectral shape does not change from 0 T to 3 T. We measured the energy resolution of 5.4-keV full-width-half-maximum at the 140-keV photopeak inside and outside of the MRI system. The MRI magnetic field and CZT electric field cause a Lorentz force on the charge carriers in the CZT [8]. In the image acquisition and reconstruction we correct for the effect of the Lorentz force [7].

## 3.2. Countrate Performance

The activity required for mouse imaging depends on several factors, including the biodistribution of the radioactive agent used and the targeted organ. In some cases the injected activity can be up to 1 mCi (37 MBq). Fig. 5 (left) shows a measurement of the system countrate ($c$) versus activity ($a$) from a $^{99m}$Tc up to 500 $\mu$Ci. We find that the countrate ($c$) fits a paralyzable detector model $c = s \cdot a \cdot e^{(-s \cdot a \cdot \tau)}$, where $s$ is the sensitivity and $\tau$ is the deadtime. The measurement shows that the countrate capability of the SPECT system is suitable for a range of activities used in *in-vivo* mouse studies.

## 3.3. Sensitivity and Spatial Resolution

We measured the system sensitivity from the countrate curves and the spatial resolution at the center of the FoV from point spread functions. For comparison we calculated the system sensitivity and spatial resolution at the center of the FoV using the equations given above. Fig. 5 (right) shows the calculated values and the measured values for three collimators with different pinhole diameters.

The calculations and the measurements agree within the uncertainties of the measurement and the calculation. We observe that the spatial resolution improves with smaller pinhole diameter while the sensitivity decreases as expected from the calculation. From the measured sensitivity for the three collimators and Eq. 2 we calculate the pinhole diameters of 1.5 mm, 1.8 mm and 2.0 mm. These results are larger than expected from the original design diameters of 0.5 mm, 1.0 mm and 2.0 mm, respectively, and might be due the accuracy of the manufacturing and the absorption of the radiation at the edges of the pinholes.

## 3.4. SPECT and MR Images

We have acquired SPECT images from a 2-dimensional (2D) point source phantom [Fig. 6 (top left)]. The phantom consists of ø1-mm point sources located at the corners of 4 triangles that are on the same plane. We acquired SPECT tomographic data using 3 different angular settings of the collimator sleeve which gives a data set of 72 projection views. We used the 72 projections to reconstruct the image of the 2D point source phantom. Fig. 6 (top right) shows the coronal image reconstructed from the 2D point source phantom. The points at 5-mm and 4-mm spacing in the triangular point pattern can be resolved and are clearly visible

in the reconstructed image. The intensity of the the points in the image varies due to activity variations in the phantom.

We filled the tubes in an ultra-micro phantom [Fig. 6 (bottom left)] with a solution of water, $^{99m}$Tc and $CuSO_4$. The phantom has 6 regions of tubes: the smallest and largest tubes have 0.75-mm and 2.4-mm diameter and separation, respectively. We placed the phantom inside the SPECT camera and moved it into the 3-T MRI system, followed by a simultaneous SPECT and MRI acquisition. We found that the structures in the ultra-micro phantom were too small to be resolved by the SPECT system with ø2-mm pinholes. The MRI system allowed us to acquire images during SPECT acquisition. Fig. 6 (bottom right) shows a 1-mm thick axial slice of the ultra-micro phantom. The MR image shows the smallest structures of the ultra-micro phantom very well, despite the SPECT system acquiring data simultaneously.

## 4. Conclusion

We have built a SPECT system for simultaneous SPECT and MRI of small animals *in-vivo*, based on MR-compatible $\gamma$–radiation detectors. We have begun testing the SPECT with $^{99m}$Tc phantoms inside the MRI and at earth magnetic field. The excellent energy resolution in the radiation sensors remains unchanged inside the 3-T MRI system (5.4 keV FWHM at the 140-keV photopeak from $^{99m}$Tc). The SPECT did not affect the gradient-echo MR images. While the results are very encouraging for the development of simultaneous SPECT/MRI technology, we observe that the 12-cm diameter permits moderate spatial resolution, only. Therefore, we are studying a system with a larger diameter and improved spatial resolution [9]. The MR-compatible SPECT technology developed in this project is not limited to pre-clinical imaging and it may be possible in the future to use the same materials and methods for developments of clinical (human) SPECT/MRI systems.

## Acknowledgments

We thank A. El-Sharkawy, W. Edelstein for MRI work. We acknowlege support from the NIH (R44 EB006712 and R01 EB008730), and the Norwegian Space Centre and the Research Council of Norway (VIT.01.06.1, BIA, 176973/I40).

## References

[1]. Wagenaar DJ, et al. Rationale for the Combination of Nuclear Medicine with Magnetic Resonance for Pre-clinical Imaging. Technol. Cancer Res. Treat. 2006; 5:4, 343–350.

[2]. Azman, S., et al. A Nuclear Radiation Detector System with Integrated Readout for SPECT/MR small animal imaging; Nucl. Sci. Symp. Conf. Rec.; IEEE. 2007; 2007. p. 2311-2317.

[3]. Meier, D., et al. Detector Readout ASICs for Digital X-ray Imaging and $\gamma$-Spectroscopy. Nucl. Instr. Meth; Proc. Imaging; 2010; 2010. subm. to

[4]. Ha S, et al. Development of a new RF coil and $\gamma$-ray radiation shielding assembly for improved MR image quality in SPECT/MRI. Phys. Med. Biol. 2010; 55:2495. [PubMed: 20371909]

[5]. Cherry, SR., et al. Physics in Nuclear Medicine. 3rded.. Elsevier Science; Saunders: 2003.

[6]. Xu, Y., et al. SPECT data acquisition and image reconstruction in a stationary small animal SPECT/MRI system; Proc. SPIE, Med. Imag. Conf.; 2010; p. 6220V

[7]. Xu, J., et al. Sparse-view Image Reconstruction with System Response Modeling for a Stationary MR-compatible Small Animal Pinhole SPECT System; Poster, Annual Meeting, Soc. Nucl. Med.; 2010;

[8]. Hamamura MJ, et al. Development of an MR-compatible SPECT system (MRSPECT) for simultaneous data acquisition. Phys. Med. Biol. 2010; 55:1563–1575. [PubMed: 20164533]

[9]. Hugg, JW., et al. Simultaneous SPECT-MRI System Design for Human Brain and Pediatric Research; World Molecular Imaging Congress; Kyoto. 2010;

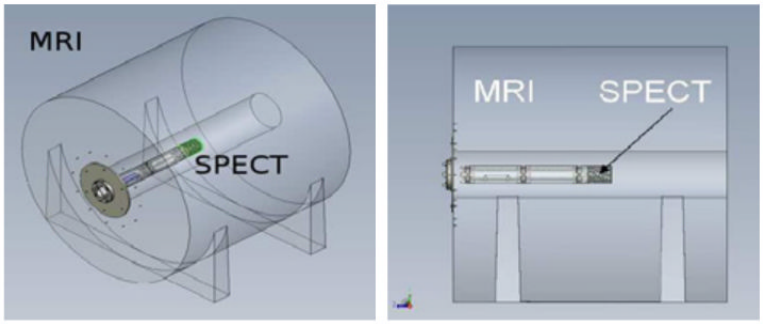


**Figure 1.**
Diagram of the small animal SPECT system inside a MRI system, 3D-view (left) and side view (right).

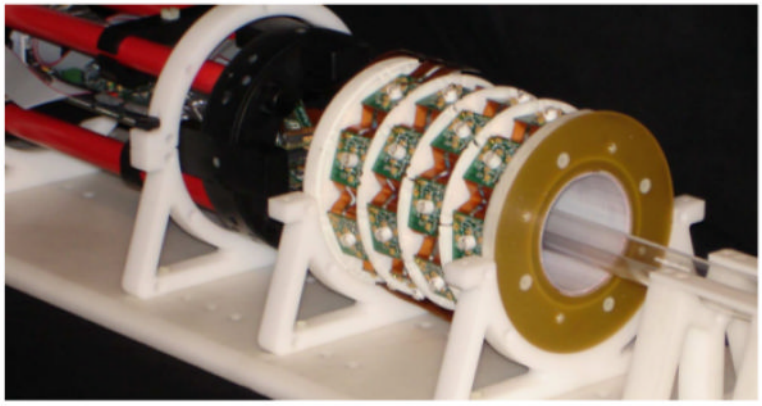

**Figure 2.**
The MR-compatible SPECT camera.

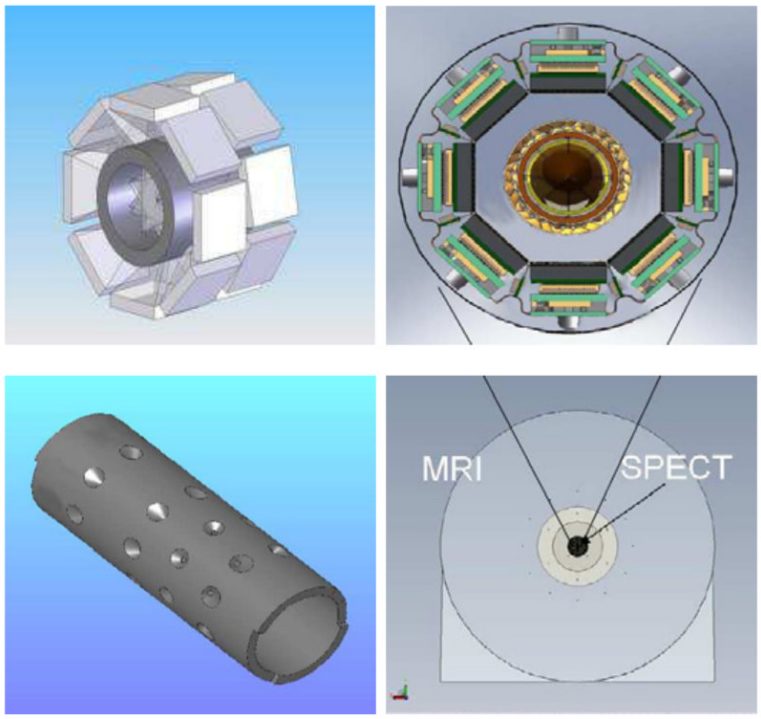


**Figure 3.**
SPECT imaging configuration: octagons of radiation detector modules are surrounding a multi-pinhole radiation collimator sleeve.

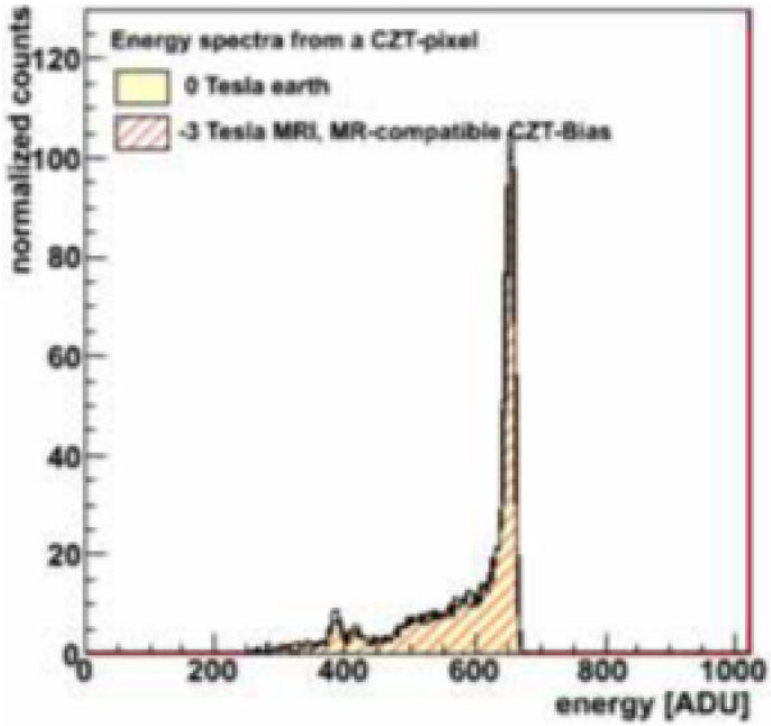


**Figure 4.**
Superimposed energy spectra from inside the 3-T MRI and at earth magnetic field.

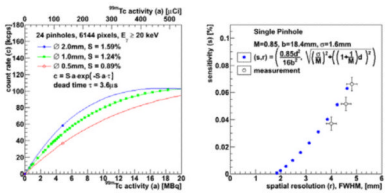


**Figure 5.**

Left: measurements (bullet points) of the countrate versus activity and fit functions (solid lines). Right: calculation (solid points) and measurement (circles) of the pinhole sensitivity vs. spatial resolution.

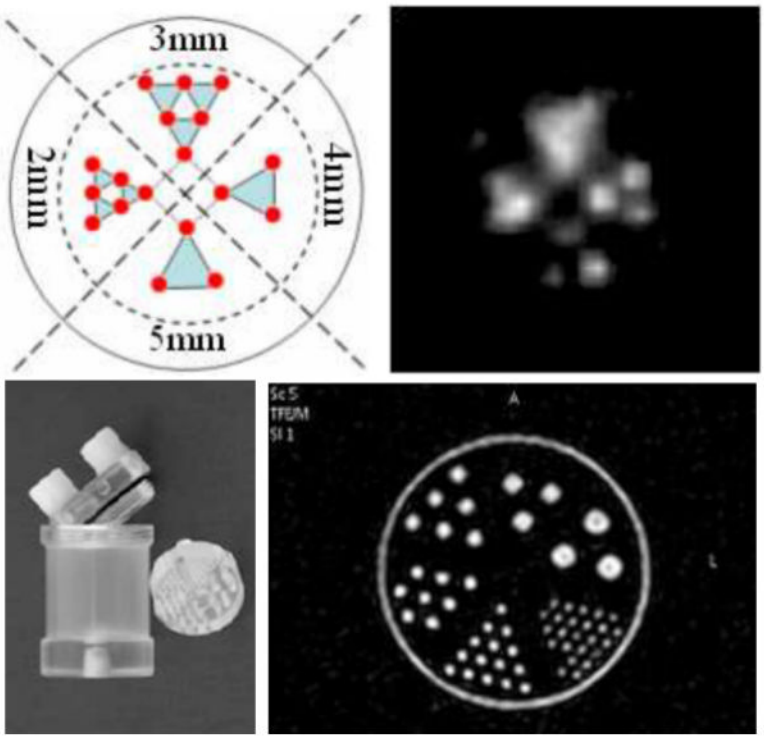


**Figure 6.**
Top: drawing of the distribution of $\gamma$-radiation point sources (left), and slices of the reconstructed image from the radiation phantom (right). Bottom: photograph (left) and axial MR image (right) of an ultra-micro phantom. The smallest white circles have a 0.75 mm diameter.

**Table 1**

Synergies of combined SPECT and MRI

| | |
|---|---|
| DCE | dynamic contrast-enhanced (DCE) imaging, MRI and SPECT combined agent |
| MC | motion correction/compensation with MRI for SPECT |
| PVC | partial volume correction with MRI for SPECT |
| AC | gamma attenuation correction with MRI for SPECT |
| AIF | arterial input function with MRI and/or SPECT |

**Table 2**

Applications for combined SPECT and MRI

| | |
|---|---|
| neurology | receptor SPECT and BOLD MRI,<br>dynamic uptake, tissue perfusion |
| cardiology | vulnerable plaques,<br>MR gated SPECT |
| oncology | oncologic processes with SPECT,<br>anatomical context with MRI |
| musculo-skeletal | injury, trauma, inflammation, fracture,<br>SPECT phosphonated agents for bone<br>MRI for cartilage, ligaments, tendon, muscle |
| therapy response | standard tests, absorption, distribution,<br>metabolism, elimination, and toxicity,<br>pharmacokinetics, pharmacodynamics |
| molecular imaging | cell labeling and tracking,<br>contrast agents for both SPECT and MRI |

**Table 3**

Preliminary specifications of the SPECT camera

| | |
|---|---|
| SPECT | SPECT/MRI simultaneously in same FOV<br>ø25-mm spherical<br>stationary system, no moving parts<br>119-mm outer diameter incl. cover<br>0.85 magnificaton (*M*) at center |
| collimator | sleeve, multi-pinhole apertures<br>one aperture per detector module<br>0.5/1/2-mm diameter keel-edge apertures (*d*)<br>tungsten-based radiation absorber |
| detector | 32 $\gamma$-radiation detector modules<br>CZT crystals, 256 anodes per crystal<br>20-keV to 360-keV energy range<br>≈ 1.6-mm FWHM intrinsic spatial resolution ($\sigma$)<br>≈ 85 % absorption ($\varepsilon$) at 140 keV<br>5.4-keV FWHM energy resolution at 140 keV |
| readout | 64 × 128-channel ASICs [3] |